THE UNUSUAL RR LYRAE POPULATION OF NGC 6101[*]

ROGER E. COHEN[1], ATA SARAJEDINI[1], KAREN KINEMUCHI[2], AND ROGER LEITON[2]
[1] Department of Astronomy, University of Florida, 211 Bryant Space Sciences Center, Gainesville, FL 32611, USA
[2] Departamento de Astronomía, Universidad de Concepción Casilla 160-C, Concepción, Chile

ABSTRACT

We use *V*-band time-series data to analyze the RR Lyrae (RRL) population of the Galactic globular cluster NGC 6101. Using template fitting, we have discovered seven new RRL stars and confirmed 10 candidates. We find unusually long mean periods for the RRL of $\langle P_{ab} \rangle = 0.803$ days and $\langle P_c \rangle = 0.393$ days, and an atypically high ratio of $n(c)/n(ab + c) = 0.82$. Based on our derived mean properties of the RRL, NGC 6101 is Oosterhoff type II, consistent with the cluster metallicity but intriguing with respect to its kinematics.

Key words: Galaxy: kinematics and dynamics – globular clusters: individual (NGC 6101) – stars: horizontal-branch – stars: variables: RR Lyrae

Online-only material: color figure, machine-readable tables

1. INTRODUCTION

Galactic globular clusters (GGCs) play a crucial role in constraining stellar evolutionary models as well as Galactic chemical evolution. Recently, many of these clusters have been the subject of greatly improved photometric studies using deep multi-color CCD observations (Piotto et al. 2002; Sarajedini et al. 2007). However, time-series investigations of these clusters remained surprisingly scarce, especially in the southern hemisphere. In some cases, clusters with recent, high-quality CCD-based color–magnitude diagrams (CMDs) remained unsearched for variables, even down to the horizontal branch (HB). To this end, we are conducting a ground-based stellar variability survey targeting GGCs which still lack deep time-series data. In this paper, we present initial results, focusing on the RR Lyrae (RRL) population of NGC 6101.

RRL stars in GGCs are of great astrophysical value for several reasons. Because of their narrow range in absolute magnitude, they function as important standard candles for extragalactic populations (i.e., Clementini et al. 2001; Sarajedini et al. 2006, see Clementini 2010 for a review of extragalactic RRL). Their light curve properties correlate with metallicity (see Sandage 2004 for an excellent discussion), serving as a check on other methods for determining the properties of their host clusters. We have conducted a time-series investigation of NGC 6101 with the goal of analyzing its RRL population.

NGC 6101 is a fairly old, metal-poor GCC. The most recent photometric investigation of this cluster by Marconi et al. (2001, hereafter M01) found $(m - M)_V = 16.12$ and an age of 12 Gyr by fitting the observed cluster sequences using a metal abundance of $Z = 0.0004$ ([Fe/H] ~ -1.7 without alpha enhancement). This distance modulus is in good agreement with values determined by Sarajedini & Da Costa (1991, hereafter SD91) via isochrone fits and a V(HB)$-$[Fe/H] calibration using a metallicity of [Fe/H] $= -1.80 \pm 0.10$, although they suggested an age of 13 Gyr via relative age-dating techniques. Reddening estimates remain somewhat uncertain, but SD91 use $E(B - V) = 0.06 \pm 0.02$ based on a compromise between reddening maps and integrated colors, and M01 adopt $E(B - V) = 0.1$. The more recent reddening map of Schlegel et al. (1998) gives $E(B - V) = 0.11 \pm 0.02$. Geisler et al. (1995) find a spectroscopic value for the metallicity of [Fe/H] $= -1.86 \pm 0.04$, leading to a value of [Fe/H] $= -1.82$ in the GGC catalog of Harris (1996, 2003 revision, hereafter H96) on the Zinn & West (1984, hereafter ZW84) metallicity scale when combined with the estimate of SD91. This is in excellent agreement with the results of M01 and Rosenberg et al. (2000), as well as those of Rutledge et al. (1997) obtained using spectroscopy of the Ca II triplet. These values are further supported by recent deep *Hubble Space Telescope* imaging from the Advanced Camera for Surveys GCC Treasury Survey (Sarajedini et al. 2007): isochrone fits to these data by Dotter et al. (2010) yield a metallicity of [Fe/H] $= -1.80$ (also on the ZW84 scale) and an age estimate of 13 ± 1 Gyr.

The only existing variability study for NGC 6101 was conducted by Liller (1981), based on 13 photographic plates observed by Alcaino (1974). Fifteen variables were identified which are included in the Clement et al. (2001) catalog of variable stars, where they are classified as RRL although periods had not been determined. Five of these (V11–15) lie much farther from the cluster center than the rest. Based on their radial distance and smaller variability amplitudes, Liller surmised that these five outliers may not be RRL or cluster members. This is indeed the case, as they all lie outside the now-known cluster tidal radius of 7.27 arcmin (H96). We have reanalyzed the other 10 candidate RRL and, based on our CMD and time-series photometry, identified seven additional RRL.

In the next section, we present the details of our observations and data reduction. In Section 3, we describe our method for determining the parameters of our RRL, place quantitative limits on the completeness of our RRL sample, and present their light curves along with a discussion of individual variables. In Section 4, we discuss the global properties of the RRL population in the context of the host cluster and other GGCs, and in the final section we summarize our results.

2. OBSERVATIONS AND DATA REDUCTION

Our ground-based observations of NGC 6101 were obtained at Cerro Tololo Inter-American Observatory with the Yale 1.0 m telescope, operated by the Small and Moderate Aperture

---

Table 1
Log of Observations

Date (UT)	Filter	Exp. Time	Number of Observations
2008 Jul 14	B	1200 s	1
	V	900 s	9
2008 Jul 15	B	1200 s	1
	V	900 s	9
2008 Jul 16	B	1200 s	1
	V	900 s	8
2008 Jul 17	V	900 s	9
2008 Jul 18	B	1200 s	1
	V	900 s	10
2008 Jul 19	V	900 s	6

Research Telescope System consortium, on the nights of 2008 July 14–19. The Y4KCAM detector was used, which has 0.289 arcsec pixel^{-1} and a field of view of 20 arcmin per side. Our time-series observations were obtained with the V filter and typically, at least one image in the B filter was obtained on each night as well so that CMDs could be constructed to aid in confirming the nature of our variables. A log of our observations in presented in Table 1.

Images were pre-processed using IRAF[3] scripts written by P. Massey for use with Y4KCAM data. Due to the crowded nature of our field, point-spread function (PSF) fitting photometry was performed with the latest version of the DAOPHOT II package (Stetson 1987), allowing for quadratic spatial variations in the PSFs. Photometry from the individual time-series frames was matched to a reference image in each filter selected based on the best seeing. To convert the mean instrumental magnitudes in each filter to standard magnitudes, we used stars in NGC 6101 from the Stetson Photometric Standard database maintained at the Canadian Astronomy Data Centre (CADC). However, since this sample did not contain any stars bluer than $B - V \sim 0.3$, the CADC standards were supplemented by the blue HB stars from M01 to broaden the color baseline used to determine the color term. Since the ground-based photometry of M01 is more precise than that of the CADC database for this cluster, we standardized our magnitudes to those of M01 for the sake of homogeneity. In summary, our set of standards is comprised of M01 magnitudes for CADC standards present in the M01 photometry, supplemented by blue HB stars from the M01 photometry. Comparing the standard magnitudes and colors between M01, who used Landolt (1992) standards to put their photometry on the standard system, and the CADC database for stars common to both in Figure 1, we find that there is essentially no systematic color offset. However, there does appear to be a fairly constant V magnitude offset between the two. Weighting each star by the inverse of the square of its photometric error, the average offset between M01 and the CADC standards is 0.025 mag. We have applied this shift to the zero point obtained using the M01 photometry to make our magnitudes consistent with the CADC standards. The resulting transformation equations, shown in Figure 2, are as follows:

$$B = b - (2.1608 \pm 0.0028) - (0.0086 \pm 0.0098)(B-V) \quad (1)$$

$$V = v - (1.6034 \pm 0.0010) + (0.0238 \pm 0.0033)(B-V). \quad (2)$$
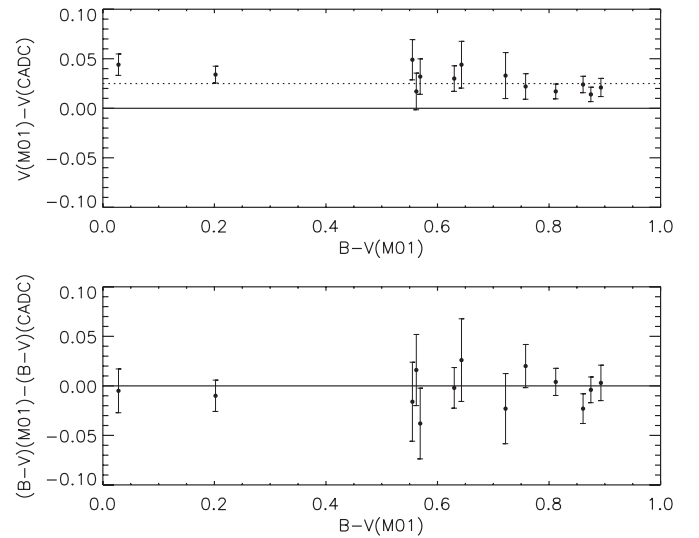
Figure 1. Color difference and V magnitude difference between M01 and standard stars from the CADC database for stars common to both. Although there does not appear to be any color offset, there is an average V magnitude offset of 0.025 mag, shown as a dotted line, which we used to offset our V magnitudes to those of the CADC standards.
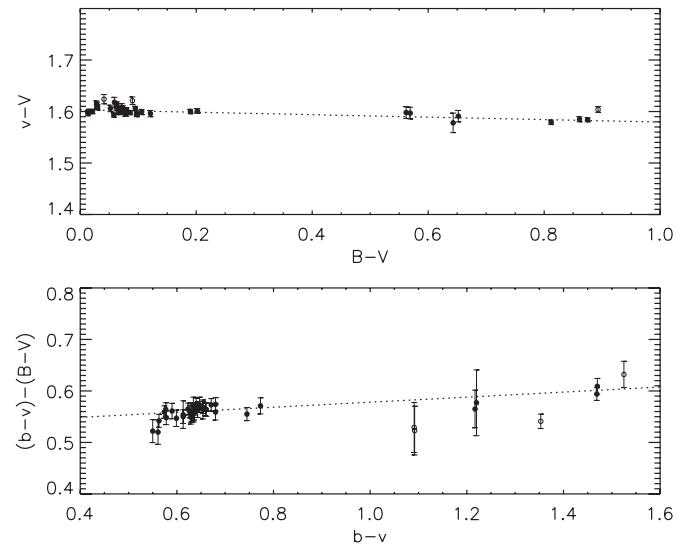

Figure 2. Standard vs. instrumental magnitude (top) and color (bottom) for secondary standards from M01. Linear fits using 2σ rejection were used to obtain the transformation coefficients, and rejected points are shown as open rather than filled circles.

We matched our photometry to that of M01 to compare our results. Since M01 only provide their positions in pixel coordinates, we matched our coordinate system to theirs using the GEOMAP and GEOXYTRAN tasks in IRAF by visually cross-referencing a small set of bright ($V < 18$) stars between images. The resulting transformation, with an rms value of 0.11 pixels, was then applied to the rest of the stars. The positional tolerance for considering a star successfully matched was determined by iterating upward in units of 0.1 pixels, and we used 1.0 pixel as our tolerance since at that value, 98% of the maximum number of matched stars were matched successfully, and below that value, the number of matched stars begins to drop off sharply with decreasing tolerances. A total of 4700 stars were successfully matched with the ground-based photometry of M01, and the difference between our computed magnitudes and colors and theirs is plotted in Figure 3 in the sense (this study)–(M01). The

Table 2
NGC 6101 RR Lyrae Properties

ID	R.A. (J2000.0)	Decl. (J2000.0)	Period	A_V	$\langle V \rangle$	$\langle B \rangle - \langle V \rangle$	[Fe/H][a]	Type
	(hh mm ss.s)	(dd mm ss.s)	(days)	(mag)	(mag)	(mag)	(dex)	
V1	16 26 02.7	−72 11 14.3	0.460	0.379	16.381	0.286	−1.99	RRc
V2	16 26 01.7	−72 13 30.4	0.412	0.443	16.440	0.184	−1.60	RRc
V3	16 26 12.3	−72 13 00.0	0.753	0.722	16.640	0.509	−1.60	RRab
V4	16 26 15.8	−72 11 53.5	0.349	0.535	16.520	0.155	−2.08	RRc
V5	16 26 29.2	−72 09 51.6	0.742	0.466	16.453	0.518	−1.51	RRab[b]
V6	16 25 50.4	−72 11 10.1	0.523	0.525	16.373	0.170	−1.49	RRc[b]
V7	16 25 19.7	−72 10 50.8	0.410	0.461	16.640	0.237	−1.66	RRc
V8	16 26 22.7	−72 11 28.5	0.419	0.453	16.532	0.251	−2.10	RRc
V9	16 25 48.3	−72 11 24.8	0.341	0.426	16.686	0.289	−0.81	RRc
V10	16 25 30.3	−72 12 48.5	0.349	0.468	16.608	0.352	−2.08	RRc
V16	16 24 45.7	−72 15 02.7	0.380	0.478	16.462	0.140	−2.13	RRc
V17	16 25 04.9	−72 07 11.2	0.417	0.192	16.224	0.434	−1.94	RRc[b]
V18	16 25 27.6	−72 16 13.8	0.427	0.421	16.397	0.469	−1.71	RRc
V19	16 25 34.0	−72 08 58.8	0.372	0.341	16.536	0.193	−1.71	RRc
V20	16 26 05.8	−72 12 12.8	0.913	0.643	16.254	0.373	−2.28	RRab
V21	16 26 57.3	−72 08 50.5	0.320	0.226	16.486	0.331	−1.99	RRc
V22	16 25 17.1	−72 11 41.3	0.320	0.100	16.505	0.281	−1.87	RRc

Notes.
[a] Based on Fourier decomposition or template fitting as described in Section 4.3.
[b] Classification somewhat uncertain, see Section 3.3 for a discussion.
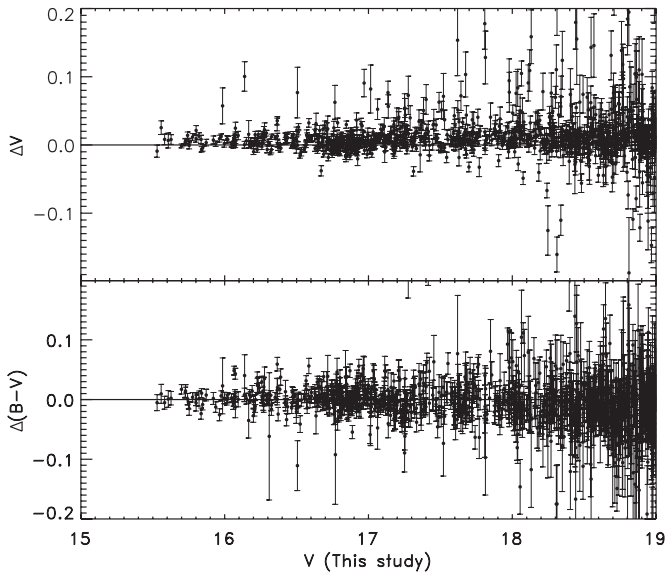

Figure 3. Differences between our magnitudes and colors and those of M01 for all stars which we were able to match, shown down to $V = 19$.

mean magnitude and color differences between our photometry and that of M01 are both under 0.005 mag.

To construct our V-band time series as well as our CMD, we only included stars which were present in at least one-third (14) of the V images and at least half (2) of the B images. Frame-to-frame variations were removed using the ensemble photometry technique of Gilliland & Brown (1988), resulting in a mean frame-to-frame rms of ∼0.004 mag for HB stars ($16 < V < 17$). After rejecting images that were either defective or had exceptionally poor seeing, 42 V-band images were included in the time series. In the following section, we describe our method for determining the variability properties of the RRL from our time series and present their light curves.

3. RR LYRAE CHARACTERIZATION

3.1. Detection and Light Curve Analysis

A periodicity search and light curve analysis were performed with the template-fitting software FITLC, described in some detail in Sarajedini et al. (2009). This software minimizes χ^2 as a function of period for each of 10 templates while allowing light curve elements such as period, amplitude, and ephemeris to vary as free parameters or be fixed by the user. The templates which can be fit consist of six RRL of ab type, two of c type (including a sinusoid), a W UMa eclipsing binary template, and an Algol-type eclipsing binary. Our candidates were initially searched for periods ranging from 0.2 to 1.0 days in steps of 0.01 days. Once an approximate period was identified for each star, it was refined by using a period increment of 0.001 days over a much narrower period range. If there were multiple deep minima in period–χ space, the period was fixed at each of the values corresponding to these minima. Of these possible periods, the period and light curve template which produced the best fit based on visual inspection was taken as correct and the corresponding set of light curve parameters was used. Since our time series consist of mostly V-band images with very few images in the B filter, the small number of B data points were fit simultaneously with the V-band light curves to allow the calculation of the intensity-weighted mean magnitude in both filters. Our phased light curves are shown in Figure 4, and the locations of the variables are displayed in Figure 5. While no RRL were detected in the central arcminute of the cluster, the results from our completeness tests in Section 3.2 imply that this is due to stochastic variations and the small number of total RRL in the cluster. This is reinforced by the fact that two of our RRL do lie within the cluster core radius, and this cluster does have a relatively low central concentration of $c = 0.80$ (H96). In Table 2, we list the properties of all of our detected RRL, including position as well as the intensity-weighted mean magnitudes and colors as determined from the template light curve fits. The mean color given here is the difference of the intensity-weighted mean magnitudes, denoted as $\langle B \rangle - \langle V \rangle$.
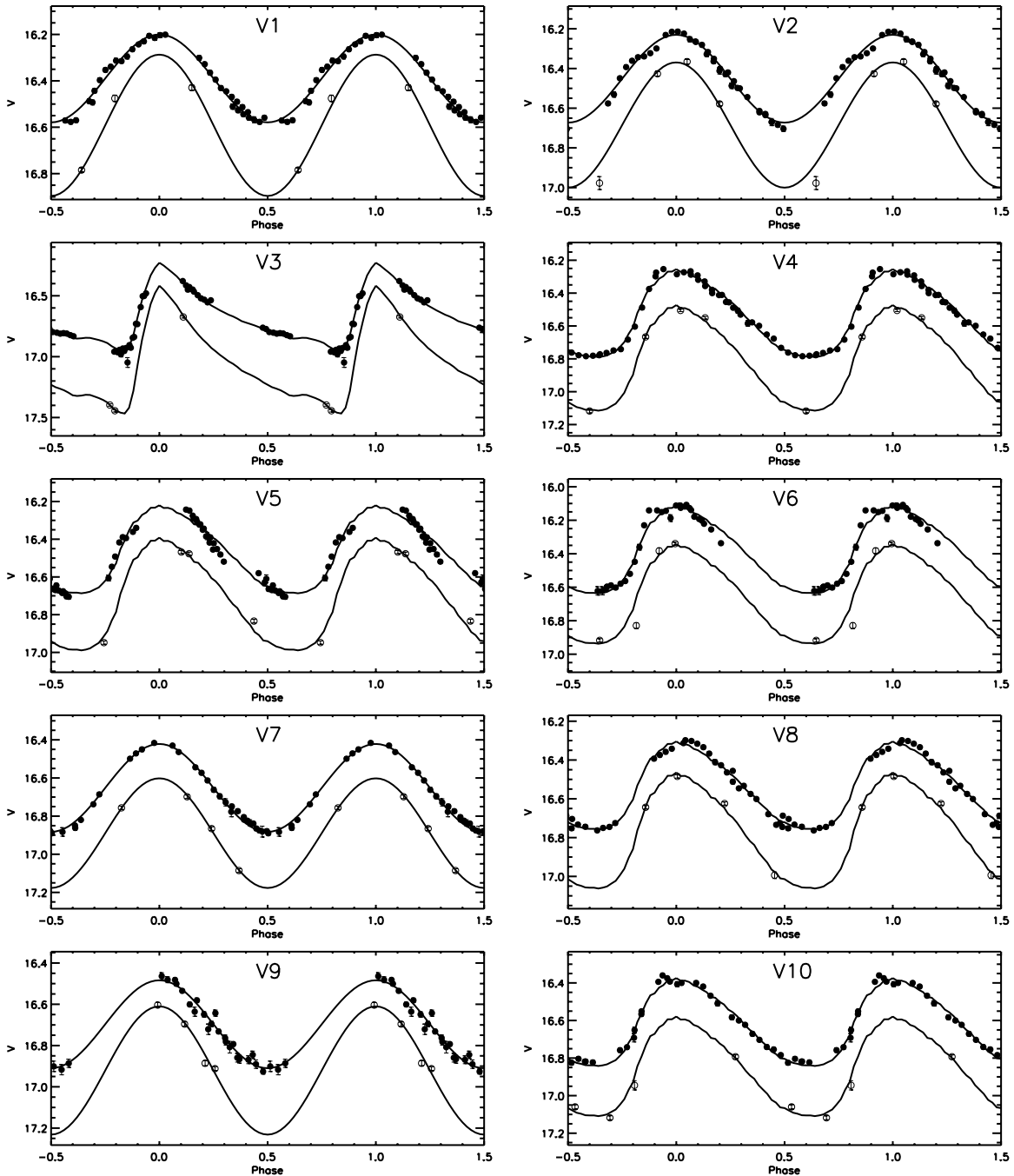
Figure 4. Phased light curves for our 17 variables, shown over two phases. Data points in the *V* filter are shown as filled circles, and *B* data points are shown as open circles. The best-fitting template for each star, used to determine period, amplitude, and mean magnitude, is overplotted as a solid line. For clarity of presentation, the data and fits in the *B* filter have been offset from the *V* time-series data by half of the *V*-band amplitude for all variables.

Bono et al. (1995) have shown that different expressions of mean color can lead to significantly different color values, and these differences are correlated with amplitude. We have chosen $\langle B \rangle - \langle V \rangle$ rather than $\langle B - V \rangle$ or $(B - V)$ because, according to their Figure 4, this expression of mean color generally differs least from the color of the "equivalent static star": it is within 0.02 of the color that the star would have if it was not pulsating except for luminous ($\log L/L_{\odot} = 1.81$) RRab with $(B - V)_0 \sim 0.32$, where it differs by up to 0.04. There is only one variable, the RRab V20, in this color range in our sample, and that potential color difference is small enough as to not significantly affect its location on the CMD in terms

of its astrophysics. Because all of our RRL have $A_V < 0.75$, we have not attempted to apply the amplitude-based corrections to the mean static values, since these corrections are all under 0.02 mag. The positions given in Table 2 were computed using a DSS image of NGC 6101 via the same method as our matching to M01. The rms deviation from our matched coordinates in this case was 0.2 arcsec. In Table 2, we also list the periods and amplitudes of the variables, followed by the Fourier phase parameter ϕ_{31} and the [Fe/H] value calculated from ϕ_{31} as discussed below in Section 4.3.

The designations are from Liller (1981) and, in order to avoid confusion with their field variables V11–V15, we have
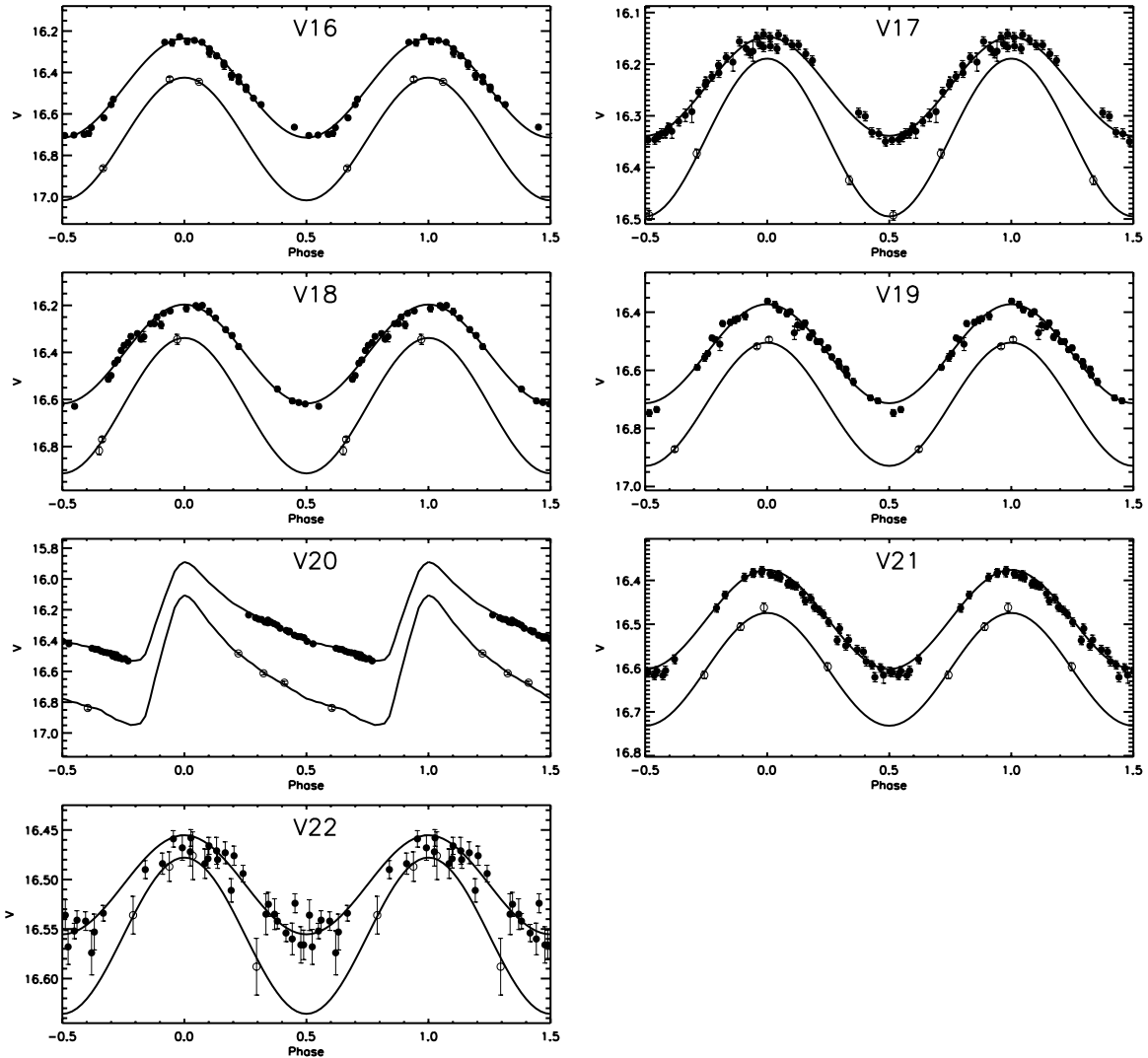
Figure 4. (Continued)

<table>
<tr><td colspan="7" align="center">**Table 3**
Photometry of NGC 6101</td></tr>
</table>

ID	x	y	$\langle B \rangle$	σ_B	$\langle V \rangle$	σ_V
1	259.262	2840.025	19.8017	0.0336	18.7028	0.0042
2	260.693	2530.222	18.6006	0.0137	17.6786	0.0020
3	260.887	2591.964	18.2402	0.0090	17.1926	0.0017
4	261.387	3906.667	17.9939	0.0061	17.2620	0.0013
5	263.586	1234.279	20.6219	0.0550	19.6732	0.0077
6	263.873	1826.292	19.8390	0.0307	19.1110	0.0047
7	264.591	798.696	20.0024	0.0350	19.5767	0.0087
8	265.555	1802.765	18.3975	0.0082	17.6504	0.0016
9	266.269	4062.393	17.4336	0.0043	16.8691	0.0012
10	266.913	3642.387	20.1354	0.0371	19.2751	0.0042

(This table is available in its entirety in a machine-readable form in the online journal. A portion is shown here for guidance regarding its form and content.)

<table>
<tr><td colspan="4" align="center">**Table 4**
V1 Time Series</td></tr>
</table>

Filter	JD -2454600	Magnitude	Magnitude Error
V	65.48228	16.301	0.0098
V	65.49402	16.328	0.0091
V	65.50532	16.365	0.0098
V	65.51714	16.395	0.0092
V	65.52843	16.431	0.0097
V	65.53973	16.445	0.0094
V	65.55136	16.469	0.0095
V	65.56265	16.490	0.0096
V	65.57408	16.513	0.0097
V	65.58580	16.535	0.0092

(This table is available in its entirety in a machine-readable form in the online journal. A portion is shown here for guidance regarding its form and content.)

designated our seven new variables V16–V22. Our photometry for the entire cluster is available electronically in Table 3, which gives the mean B and V magnitudes and their errors for all the stars in our field of view which were detected in at least one-third of the V images and one-half of the B images. Additionally, the time-series observations for the individual variables V1–V10 and V16–V22 are available in Table 4.

3.2. Completeness

3.2.1. Random and Systematic Errors

Our cluster CMD, along with σ_V, the standard deviation of the frame-to-frame variations, is shown in Figure 6 for stars included in our time-series photometry. In an effort to clean our CMD and examine the effects of crowding on our photometry,
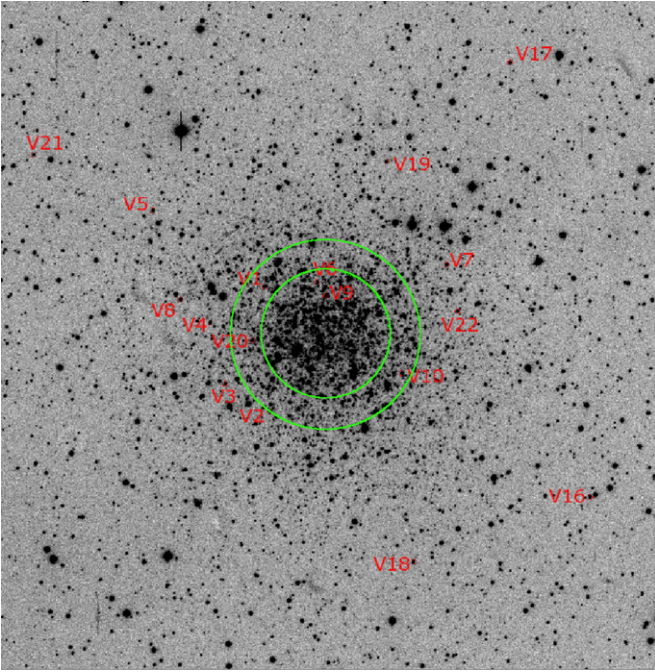
Figure 5. Locations of all of our variables, including V1–10 from Liller (1981). North is up and east is to the left. This image is a raw (non-PSF subtracted) 12 arcmin per side portion of our 20 arcmin field of view. Variables are circled and labeled in red, and the inner and outer green circles indicate the core and half-mass radii, respectively, taken from H96.

(A color version of this figure is available in the online journal.)

all stars within the cluster tidal radius of 7.27 arcmin (H96) are plotted as small points, while only stars within the cluster half-mass radius of 1.71 arcmin (H96) are plotted as large points, with the exception of the detected RRL, which are plotted as crosses regardless of radial location in the cluster.

As a first step in quantifying our ability to successfully recover the light curves of variables, we have attempted to characterize the contribution of random and systematic errors to the total frame-to-frame standard deviation of cluster stars shown in the right-hand plot of Figure 6. This was done by fitting a function in the log σ_V–V plane to all stars within the cluster radius. Based on inspection of the right-hand plot of Figure 6, this function consists of a constant for stars brighter than a certain cutoff magnitude, and a line for stars fainter than that magnitude. Allowing the constant (for the bright portion), slope and offset (for the faint portion), and cutoff magnitude to vary as free parameters, we performed our fit iteratively rejecting stars outside 2σ from the fit until the fit parameters changed by less than 1%. The resultant cutoff magnitude is $V = 17$, and we can see that for stars brighter than this magnitude, the lower envelope of σ_V is approximately constant, and presumably represents the systematic contribution to the total standard deviation. In our case, we can see that this systematic contribution is due mostly to our frame-to-frame rms deviation of 0.004 mag. Thus, we shifted our fit by −0.403 in log space so that the constant portion of our fit was set by this systematic contribution, thereby using the fit to determine the predicted error "floor" above which contributions to σ_V may be due to actual intrinsic variability. For stars with $V > 17$, the slope of this line is 0.29, higher than the slope of
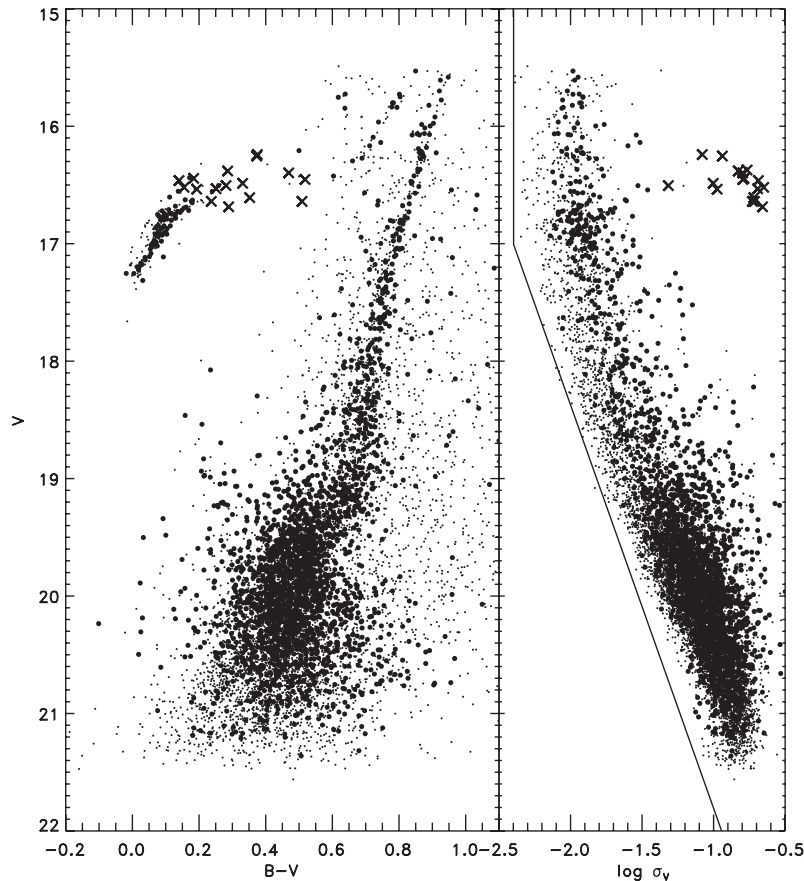

Figure 6. Color–magnitude diagram (left) and frame-to-frame standard deviation (right) plotted for all stars within the cluster tidal radius (small points) and half-mass radius (large points). The solid line in the right-hand figure indicates the contribution from random and systematic errors in our photometry, see the text for a discussion.
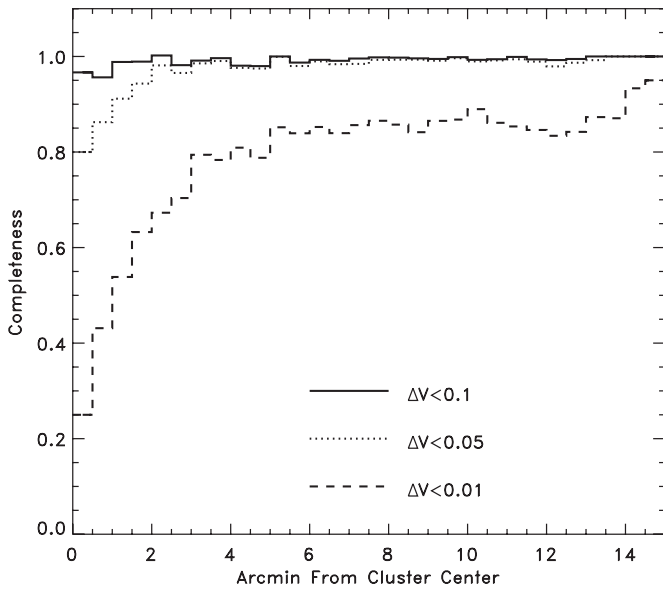
Figure 7. Fraction of artificial HB stars recovered within different magnitude tolerances as a function of radius from the cluster center.

Figure 8. Difference between input and output periods as a function of output period for our 400 simulated RRL. Symbols (other than filled circles) mark variables recovered with the wrong type of template: RRab recovered as RRc or W UMa are indicated by diamonds and squares, respectively, RRc recovered as RRab or W UMa are indicated by triangles and crosses, respectively, and WUMa recovered as RRab or RRc are indicated by open circles and pluses, respectively.

0.2 which would arise from solely Poissonian noise, implying that crowding has some influence on our photometry. The effect of crowding can also be seen over the entire magnitude range of our photometry in that stars with $r < r_{hm}$ have a higher error "floor" than the stars with $r > r_{hm}$. For this reason, we have conducted a series of tests to quantify the influence of crowding on our ability to detect RRL.

3.2.2. Artificial Star Tests

Since NGC 6101 has a relatively small number of RRL, it is crucial to determine whether there may be any RRL which we have failed to detect. There has been much recent evidence that, in extremely crowded fields, image subtraction methods such as the ISIS package (Alard 2000) are more successful at producing accurate light curves of variable stars than PSF subtraction methods (e.g., Figure 2 of Székely et al. 2007). However, based on inspection of our PSF-subtracted images and the relatively low central concentration of NGC 6101 ($c = 0.8$ according to H96), we decided to test our hypothesis that for the RRL, which have high signal-to-noise in our data, crowding is not a significant issue, even at the center of the cluster. We added 2500 artificial stars to each of 10 pairs of B- and V-band images, with the stars gridded evenly across the image and separated by four times the PSF radius to prevent neighboring artificial stars from influencing each others' photometry (although, importantly, their photometry will be influenced by the real stars and vice versa). These stars were randomly assigned magnitudes and colors corresponding to the HB region of the CMD ($16.5 < V < 17.3$, $0 < B - V < 0.5$). A star was considered successfully recovered if its position was within 4 pixels (the approximate median seeing in our images) of the input position (in practice all stars were recovered within 1 pixel of their input positions), and its output magnitude was within a certain chosen magnitude tolerance of its input magnitude. To assess the effect of crowding on the DAOPHOT photometry, we plot the fraction of input HB stars recovered as a function of distance from the center of the cluster for different allowed magnitude tolerances in Figure 7.

It is clear that crowding in the core has an effect on photometric precision, and even at large radii, our frame-to-
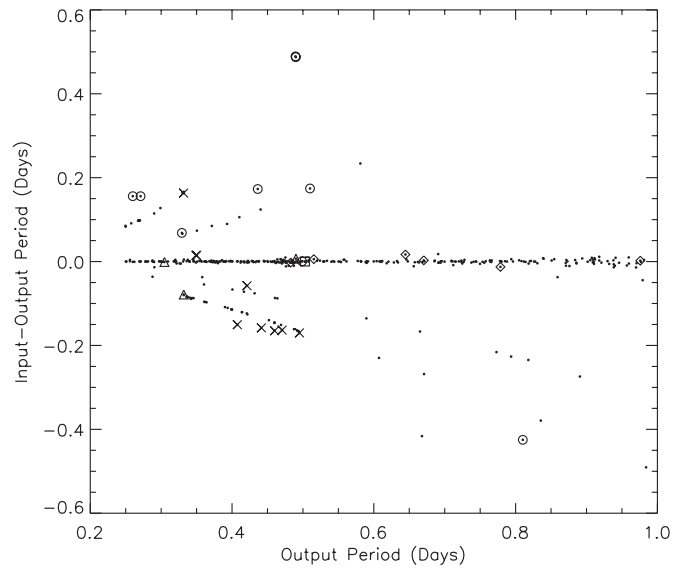
frame rms prevents 10%–20% of the stars from being measured to within 0.01 mag. However, even in the central 1 arcmin of the cluster, over 80% of the input HB stars were recovered with magnitude deviations under 0.05 mag. While this would cause scatter in the detected light curves and presumably hamper the detection of low-amplitude variables, we can use simulations to assess the influence of this level of scatter on our ability to recover RRL light curves.

3.2.3. Simulations

We have tested the ability of our template-fitting software to recover RRL by creating simulated variables. This was done by sampling template light curves at the actual epochs of our observations. Four hundred input variables consisting of 100 RRab, 200 RRc (100 with the RRc template and 100 with the pure sinusoid), and 100 WUMa, were randomly assigned periods (P) and amplitudes (A_V) as follows based on Figure 4 of Cacciari et al. (2005): RRab were assigned $0.45 < P < 1.0$ days and $0.1 < A_V < 1.5$, RRc were assigned $0.25 < P < 0.5$ days and $0.1 < A_V < 0.8$, and W UMa binaries were assigned $0.25 < P < 1.0$ days and $0.1 < A_V < 1.0$. To quantify whether RRL light curves can be recovered despite crowding in the center of the cluster, the variables were given mean magnitudes corresponding to our faintest observed RRL ($\langle V \rangle = 16.686$), and the individual observations were all separately offset by a random amount drawn from a Gaussian distribution centered on a mean photometric error of 0.05 mag. In Figure 8, we plot the difference between input period and recovered period as a function of recovered period.

Of our 400 input stars, only 29 of them (7%) were recovered with the wrong type of template (i.e., the best fit was to a template other than the input template). These stars are overplotted in Figure 8 with different symbols corresponding to different input and output templates, and the largest contribution to this group comes from the RRc, nine of which were recovered as binaries. To quantify our ability to recover RRL at the correct period, we
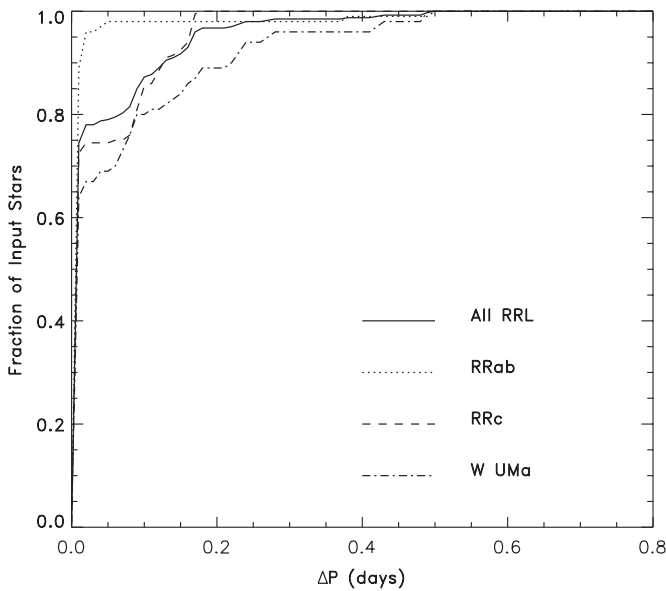
Figure 9. Fraction of recovered variables as a function of difference between input and output period. The dotted line corresponds to the RRab, the long dashed to the RRc, the dot-dashed line to the WUMa binaries, and the solid line represents the aggregate of all of the variables.

have plotted the fraction of recovered input stars as a function of the difference between input and output periods in Figure 9, for the entire sample as well as for the different types of variables.

We can see that, using the template-fitting method, RRab are recovered more easily at the correct period than RRc or W UMa binaries, most likely due to their generally larger amplitudes and less sinusoidal light curves. Over 80% of stars are recovered at periods within 0.1 days of their true period, and of the others, 70% were recovered with fit amplitudes within 10% of their input amplitudes, implying that they are likely to at least be detected as variables. These simulations show that even in the core of the cluster, where the effects of crowding dictated our input photometric errors for the simulations, 92% of variables with periods and amplitudes typical of RRL would be at least detected as such, and the chance of a variable being misclassified is on the order of a few percent depending on the type of variable.

A purely empirical way to quantify the likelihood that there are RRL which we have failed to detect is by comparing our photometry with the photometry of M01. Although their field of view is smaller than ours, it is also centered on the core of the cluster. Their photometry extends deeper than ours, and was obtained under better seeing conditions with better spatial resolution, and according to their Figure 7, is complete down to the main-sequence turnoff. Conservatively selecting the HB region of the CMD as that with $16 < V < 18–2(B − V)$, $(B − V) < 0.7$, and $V > 15.5$ (our saturation limit) and restricting our analysis to the central 2 arcmin of the cluster, where crowding effects are apparent in our completeness tests, we were able to detect and match to their photometry 98 of 106 (92%) of their HB stars. Since we have detected seven RRL within that radius, it is unlikely that we have failed to detect additional RRL. Furthermore, if we restrict the above analysis to the central 0.5 arcmin of the cluster, we have detected and matched all 19 of the HB stars detected by M01, all of which are recovered with mean V magnitudes within 0.05 mag of those reported by M01.

In summary, our completeness tests have shown that in the central 0.5 arcmin of the cluster, where detection of RRL is most likely to be hampered by crowding, we can detect 80% of the HB stars to within 0.05 mag. Our simulations have shown that, even when limited to this level of photometric precision, 92% of RRL will be detected, and one of our detected RRL at most is likely to be misclassified by the template-fitting program (V6 is a likely example, see the discussion in the next section). Comparison to the (complete) photometry of M01 strongly suggests that in practice, this percentage is even higher, and based on the actual number of HB stars in NGC 6101, it is unlikely we have failed to detect any RRL. However, some of our detected variables had ambiguous and/or unusual results based on their template fits, and we will now discuss those variables individually.

3.3. Individual Variables

V5. We could not obtain a satisfactory fit for this variable with any of the templates. When phased with the best period, 0.75 days, the light curve appears somewhat akin to that of an ab-type RRL but the best-fitting template, by a small margin, is the sinusoid. We suspect that it may be an ab-type exhibiting the Blazhko effect, in which case phase and/or amplitude modulation would explain the lack of correspondence to any of the templates. Our data are insufficient to detect changes in light curve shape over time or determine whether the periodogram shows a closely spaced (period ratio = 0.95–1.05) doublet or triplet in the power spectrum which is characteristic of Blazhko variables. However, if this is a Blazhko RRab, then it is the only one out of three RRab in NGC 6101. This fraction of Blazhko RRab is consistent with a study of OGLE-1 data by Moskalik & Poretti (2003), who found that ∼23% of RRab and ∼3% of RRc exhibit the Blazhko effect in the Galactic bulge. However, Jurcsik et al. (2009, and references therein), having found the Blazhko effect in 14 out of 30 nearby field RRL, point out that these percentages should be viewed as lower limits in the sense that the light curve modulations associated with the Blazhko effect can occur with very small (mmag) amplitudes and most variability surveys simply lack the photometric precision to detect it. In fact, Kolenberg et al. (2010) placed a lower limit of 40% on the fraction of Blazhko RRab, and in GGCs, ∼30% of RRL exhibit the Blazhko effect (e.g., Corwin & Carney 2001; Piersimoni et al. 2002) although this is still consistent with our small data set. In any case, since our phase coverage at the best-fitting period is insufficient to detect the maximum of the light curve, our derived light curve amplitude for this variable should be regarded as uncertain.

V6. The RRc template fits the data nearly as well as the RRab template, with nearly the same period (0.519 days instead of 0.523 days), and the W UMa binary template also produces a plausible fit at a period of 0.700 days. We show all three fits for comparison in Figure 10, along with their periods, mean magnitudes, and mean colors. Given the metallicity of this cluster and the distribution of the RRab and RRc on the period–amplitude diagram (discussed later in Section 4.4), it seems extremely unlikely that V6 is an RRab. To clarify whether it is a long-period RRc or a binary, we have used the binary modeling program NIGHTFALL[4] to try and optimize the fit by allowing the binary parameters to vary beyond the generic W UMa template used in our template-fitting program. We were ultimately unable to improve the fit, even using the optional detailed reflection treatment. The fact that the W UMa template produces even a marginal fit at a period significantly longer than that fit for the RRab or RRc templates is probably an artifact of the template-fitting program:
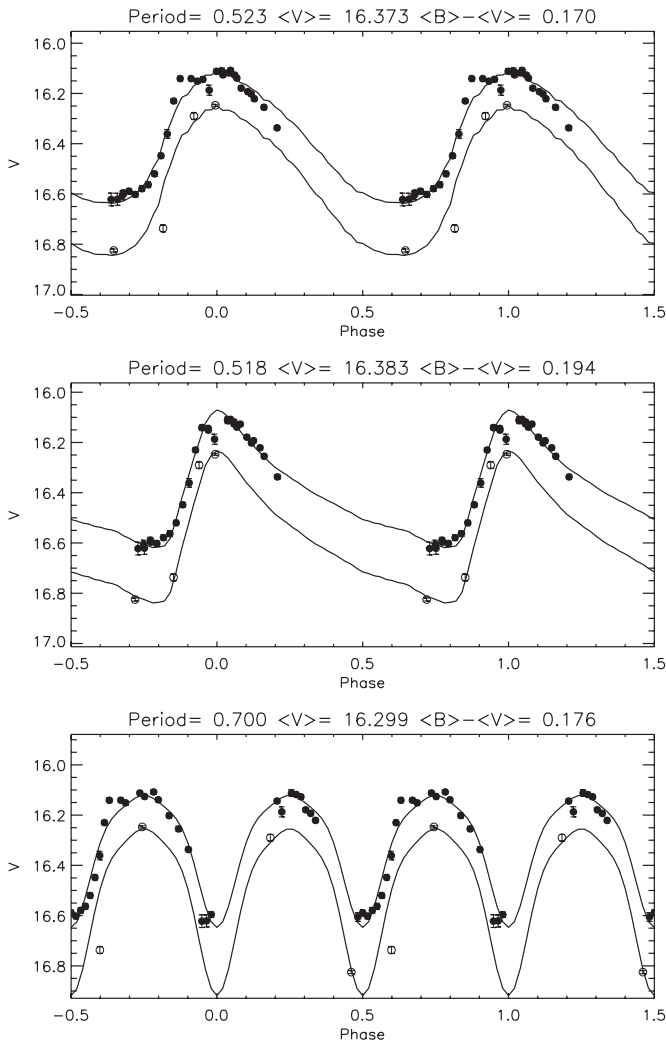

Figure 10. Time-series data for V6 fit to (from top to bottom) the RRab, RRc, and W UMa templates, with the periods, mean magnitudes, and mean colors of the best fits shown above each plot. Observations in the V filter are shown as filled circles and those in the B filter are shown as open circles, along with the best-fitting template light curves in each filter plotted as solid lines.

our simulations show that, using χ^2 minimization, RRc have a tendency to masquerade as binaries, aliased to longer periods (see Figure 8). We are left to conclude that, although unusual, the most likely scenario is that V6 is one of a very small number of unusually long-period ($P > 0.45$ days) RRc. Catelan (2004) suggests that the long periods of these RRc, also found in ω Cen, NGC 6388, NGC 6441, and M3, are related to the fact that they are relatively luminous because their host clusters have unusually bright HBs. At $\langle V \rangle = 16.373$, V6 is indeed the most luminous RRc in the cluster, second only to the similarly ambiguous V17 and the RRab V20, the latter of which has poor phase coverage which may affect its calculated mean magnitude. One more clue is provided by the light curve of V6: when phased as an RRc, there is a bump visible in the light curve just before maximum light which is also seen in the models of Bono et al. (1997) for certain mass–luminosity–temperature combinations. The light curves of the most luminous ($\log L/L_\odot = 1.91$) RRc in their Figure 5 also show this bump and bear a striking resemblance to the light curve of V6, supporting our classification as an RRc, although this bump can also occur at lower luminosities as well, albeit over a specific

range of masses and temperatures. For example, a similar bump is also present in the light curves of V4 and V10, which are less luminous than V6. Hence, for our analyses of the RRL population in the context of its mean properties in Section 4, we will include V6 as an RRc.

V17. The W UMa template produced the best results, at a period of 0.841 days. However, given the location of this star on the CMD as well as the shape of the light curve, it is improbable that this star is actually a binary system in the cluster. If one of the components is an HB star, the only other plausible location of the other component on any of the cluster sequences is near the main-sequence turnoff, and this would result in a temperature difference incapable of producing the eclipses of nearly equal depth seen in the light curve. If we hypothesize that the secondary eclipse is not observed and phase the observations of this star with half of its best-fitting period, the resultant light curve bears no resemblance to that of a close binary since the would-be primary eclipse is much too wide. The only other template that produces a tolerable fit is that of the RRc, at a period of 0.417 days. As with V6, it is possible that this star is a field interloper and/or an anomalous Cepheid, and in the latter case the shape of the light curve indicates that it is likely pulsating in the first overtone mode (see Figure 4 of Soszyński et al. 2008). However, unlike V6, the amplitude of the light curve is much smaller than that typical of anomalous Cepheids. Hence, we will consider this star an RRc, and its nature will be definitively resolved by further monitoring.

V20. One of the RRab templates produces a tolerable fit, while none of the other types of templates produced a remotely satisfactory fit. This star is most likely an RRab but, due to the poor phase coverage, the amplitude remains somewhat uncertain.

4. GLOBAL RR LYRAE PROPERTIES

4.1. Color–Magnitude Diagram: RRL and the ZAHB

The location of the RRL variables on the HB is shown in Figure 11. In general, the RRc tend toward the blue edge of the instability strip while the RRab tend toward the red edge as expected. However, one of the RRc (V18) has $\langle B \rangle - \langle V \rangle = 0.469$, although there is nothing else about the pulsational properties or light curve fit that would lead us to question its classification as an RRc: only one of the 100 RRab in our simulations was misidentified as a (smaller amplitude) RRc, and in that case, the input RRab period was nearly identical to the recovered RRc period, and the existence of an RRab in this cluster with $P \sim 0.43$ days is extremely unlikely.

Considering the RRL population as a whole, many of the RRc are slightly more luminous than the HB stars according to Figure 11, likely indicating that they are more evolved. We may test this hypothesis using Equations (4) and (5) from Cassisi & Salaris (1997) to determine the magnitude difference between $\langle V \rangle_{\rm RR}$ and the zero-age horizontal branch (ZAHB), which depends on cluster metallicity. As discussed by Sandage (1990), the spread in HB magnitudes due to evolved RRL can hamper an accurate determination of the average cluster HB magnitude, and this "thickness" of the HB is correlated with metallicity (Catelan 1992). There are two equations in Cassisi & Salaris (1997, hereafter CS97) which relate metallicity to $\langle V \rangle_{\rm RR} - V_{\rm ZAHB}$ using an HB thickness–metallicity correlation, and we may use these equations to predict a value of $V_{\rm ZAHB}$. One of the equations is in terms of [Fe/H] and one is in terms of [M/H]. If we adopt the H96 value of [Fe/H] and determine
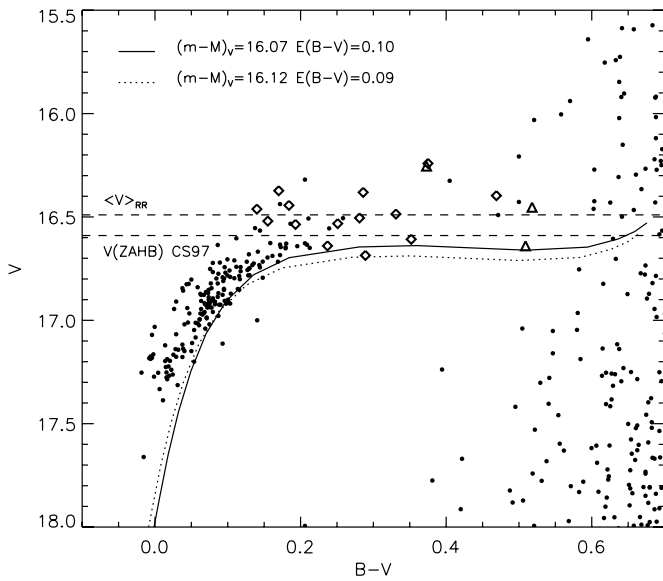
Figure 11. Enlargement of the HB region of our color–magnitude diagram for NGC 6101, showing only stars with $\sigma_V < 0.05$ within the cluster tidal radius present in at least one-third of the V frames and half of the B frames. The mean colors and magnitudes of the RRab, as defined in Section 3.1, are overplotted as triangles and the RRc are overplotted as diamonds. The solid line is the ZAHB from the models of VandenBerg et al. (2006) with $Z = 0.0004$, fit using $(m - M)_V = 16.12$ and $E(B - V) = 0.09$, and the dotted line is the same ZAHB, but shown with $(m - M)_V = 16.07$ and $E(B - V) = 0.10$. The dashed horizontal lines indicate the observed mean magnitude of the RRL and the ZAHB magnitude predicted by the CS97 relations.

[M/H] by assuming $[\alpha/\mathrm{Fe}] = 0.28$ following Ferraro et al. (1999), we obtain two resultant values, one from each expression of the metallicity. Averaging these two values of -0.11 and -0.09 gives $\langle V \rangle_{\mathrm{RR}} - V_{\mathrm{ZAHB}} = -0.10 \pm 0.03$. Adding this value to our observed $\langle V \rangle_{\mathrm{RR}} = 16.48 \pm 0.03$ yields $V_{\mathrm{ZAHB}} = 16.58 \pm 0.04$, in accord with estimates for V_{HB} of 16.6 ± 0.2 from SD91 and Rosenberg et al. (2000) and 16.59 ± 0.10 from M01. However, since the CS97 relations have a fair degree of scatter, we may also fit a synthetic ZAHB to our data. In addition to comparing the resultant ZAHB value to the value predicted by the Cassisi & Salaris (1997) relation, an empirical ZAHB fit can also yield reddening and distance modulus values.

4.2. Distance and Reddening

Using the HB, we may calculate the distance modulus via two methods. The first is by fitting a synthetic ZAHB to the observed blue HB, which can also yield a reddening value, and the second involves the use of an RRL luminosity–metallicity calibration. We will conduct this analysis using the hypothesis that the metallicity value given by H96 is correct, and then test this assumption afterward, when discussing the cluster metallicity. To perform the ZAHB fit, we have chosen to use the recent models of VandenBerg et al. (2006) with *BVRI* color–T_e relations as described by VandenBerg & Clem (2003). These model grids have the advantage that they contain ZAHBs which can be easily converted to the observational plane, and these ZAHBs have better mass and metallicity resolution than the ZAHBs produced by the more recent HB evolutionary tracks of Dotter et al. (2008). To perform the ZAHB fit, we use the models with $Z = 0.0004$ and $[\alpha/\mathrm{Fe}] = 0.3$ (Ferraro et al. 1999), corresponding to $[\mathrm{Fe}/\mathrm{H}] = -1.84$, although the model with the next highest metallicity value of $[\mathrm{Fe}/\mathrm{H}] = -1.71$ produces a very similar ZAHB which would affect the derived

reddening and distance moduli by under 0.01 mag. A fit to the observed lower envelope of the blue HB, shown as a dotted line in Figure 11, results in $(m - M)_V = 16.12 \pm 0.03$ and $E(B - V) = 0.09 \pm 0.01$, where the errors reflect the observed scatter in the lower envelope of the HB. This fit is also consistent with the faint end of the RRL magnitude distribution and indicates that most of the RRL in NGC 6101 have evolved away from the ZAHB. This is to be expected to some extent, since Ferraro et al. (1999) point out that HB stars initially evolve away from the ZAHB quite rapidly.

In Figure 11, we show our observed $\langle V \rangle_{\mathrm{RR}}$ as well as the ZAHB value predicted by the CS97 relations. Based on Figure 1 of Catelan (1992), an HB spread of at least $\Delta V \sim 0.3$ mag would be typical given the metallicity of NGC 6101, and in fact the mean magnitudes of the RRL range over 0.43 mag. This results in a discrepancy of ~ 0.12 mag between the ZAHB which we have fit to the observed HB stars and the ZAHB value predicted by the CS97 relations, which we attribute the scatter in those relations. However, it is also important to note that the ZAHB magnitude employed in the CS97 relations is based on the observed lower envelope of the HB, which is not necessarily the same as the true ZAHB. While the magnitude which represents the lower observed envelope of the HB is expected to deviate from the true ZAHB value at both the low and high ends of the GGC metallicity range (Catelan 1992), it appears that NGC 6101 falls in the metal-intermediate range of clusters for which the lower observed HB envelope is coincident with the ZAHB. This is supported by the fact that our ZAHB fit, which is based on the blue HB, is consistent with the observed RRL magnitude distribution and results in distance modulus and reddening values in good agreement with literature values.

We may now compare the distance modulus from the ZAHB fit to that obtained from an RRL luminosity–metallicity calibration. The $M_V - [\mathrm{Fe}/\mathrm{H}]$ calibration of Chaboyer (1999) relies on the RRab, and of our three RRab, one is likely a Blazhko variable and one has poor phase coverage, rendering their amplitudes (and hence $\langle V_{ab} \rangle$) somewhat uncertain. However, we may use the calibration of Tammann et al. (2008) for evolved RRL, which allows the use of all of the RRL, including the fractionally large population of RRc, and takes into account the nonlinear relationship between luminosity and metallicity:

$$M_V = 1.109 + 0.6[\mathrm{Fe}/\mathrm{H}] + 0.14[\mathrm{Fe}/\mathrm{H}]^2. \quad (3)$$

Using our measured $\langle V_{\mathrm{RR}} \rangle = 16.48 \pm 0.03$ and the H96 value of $[\mathrm{Fe}/\mathrm{H}] = -1.82$, conservatively assigning an uncertainty of ± 0.1, the resulting distance modulus is $(m - M)_V = 16.00 \pm 0.03$. While this value is slightly lower than some previous estimates (and the value resulting from the ZAHB fit), it is reasonably consistent with the value of 16.07 ± 0.1 reported by H96 based on the V_{HB} calibration used in that study as well as that of SD91. To determine a distance modulus value to use in our subsequent analyses, we have performed a weighted average of previously known values and the values which we derived: 16.07 ± 0.1 from the H96 $V(\mathrm{HB})$–$[\mathrm{Fe}/\mathrm{H}]$ calibration, 16.12 ± 0.1 from that of SD91, 16.12 ± 0.1 from M01, 16.12 ± 0.03 from our ZAHB fit, and 16.00 ± 0.03 from the above $\langle V_{\mathrm{RR}} \rangle$–$[\mathrm{Fe}/\mathrm{H}]$ calibration. This results in a distance modulus of 16.07 ± 0.02, which, when applied to our synthetic ZAHB, is most compatible with the observed HB lower envelope if we increase the reddening slightly to $E(B - V) = 0.10$. This ZAHB fit is shown as a solid line in Figure 11, and the slightly higher value of $E(B - V)$ is still within the uncertainties of other reddening estimates. Additionally, this fit is compatible

with the magnitude and color of the faintest observed RRL to within the uncertainties. Furthermore, our reddening value agrees well with the location of the RRab on the CMD: Sandage (2006) predicts a value for the fundamental blue edge of the RRL instability strip of $(B - V)_0 = 0.24$ for [Fe/H] = -1.82 (H96).

4.3. Metallicity

As a check on previous metallicity determinations for NGC 6101, we can apply the period–metallicity relationship for GGCs from Sandage (1993):

$$\log\langle P_{ab}\rangle = -0.121([Fe/H]) - 0.431 \quad (4)$$

$$\log\langle P_c\rangle = -0.119([Fe/H]) - 0.670. \quad (5)$$

Since there are only three RRab in our sample, small number statistics hamper any conclusions based on their mean period. However, we can use our 14 RRc and again test the H96 metallicity value of [Fe/H] = -1.82 ± 0.1. This yields $\langle P_c\rangle = 0.352 \pm 0.010$, lower than our observed $\langle P_c\rangle = 0.393 \pm 0.015$. Figure 3.10 of Smith (1995) shows that the correlation between RRc period and cluster metallicity has a large degree of scatter such that the periods of the RRc at a given metallicity are spread over a period range of about 0.1 days. Viewed in this context, the periods of the RRc in NGC 6101 are long, but not significantly outside the period range expected, for the cluster metallicity.

We can also use the CMD to verify the metallicity of NGC 6101. While our saturation limit of $V \approx 15.5$ prevents us from making use of many of the red giant branch (RGB) diagnostics such as $\Delta S_{2.0}$, $\Delta S_{2.5}$, or $\Delta V_{1.1}$, or $\Delta V_{1.2}$, we can use $(B - V)_{0,g}$, the dereddened color of the RGB at the height of the HB. Using the ZAHB magnitude and $E(B - V)$ values from our synthetic ZAHB fit of $V_{ZAHB} = 16.59 \pm 0.03$ and $E(B - V) = 0.09 \pm 0.03$, there are several different relations between [Fe/H] and $(B - V)_{0,g}$ which we may use. Using Equation (1) of Sarajedini & Layden (1997), we obtain [Fe/H] = -1.84 ± 0.08. If we use Equation (4.4) of Ferraro et al. (1999) and Equation (7) of Carretta & Gratton (1997) to transform to the ZW84 metallicity scale, we obtain [Fe/H] = -1.81 ± 0.2. Alternatively, if we again adopt $[\alpha/Fe] = 0.28$, we can use Equation (4.11) of Ferraro et al. (1999) and get [Fe/H] = -1.80 ± 0.19 on the ZW84 scale. All three of these values are in excellent agreement with each other and literature values, serving to reinforce our results in the previous section.

Fourier decomposition of RRL light curves can also yield metallicities based on observed correlations between Fourier phase and/or amplitude parameters and [Fe/H] values. In the case of the RRc, Morgan et al. (2007) derived a relationship between the Fourier phase parameter ϕ_{31} (formulated in this case using a cosine series), the period, and [Fe/H] values of both ZW84 and CG97. We used the light curves of our RRc to predict metallicity values on the ZW84 scale based on Equation (3) of Morgan et al. (2007), employing an eighth-order fit in all cases except V6, V9 and V22, for which the data were more sparse and a fifth-order fit was used instead. It is evident from the spread in the resultant [Fe/H]$_{ZW84}$ values in Table 2 that the quality of our data is not always sufficient for this to be a practical method of obtaining an additional metallicity estimate. Specifically, the [Fe/H] values, weighted using the inverse squares of their uncertainties, have a weighted mean of -2.07, but their median is -1.87 and their standard deviation is
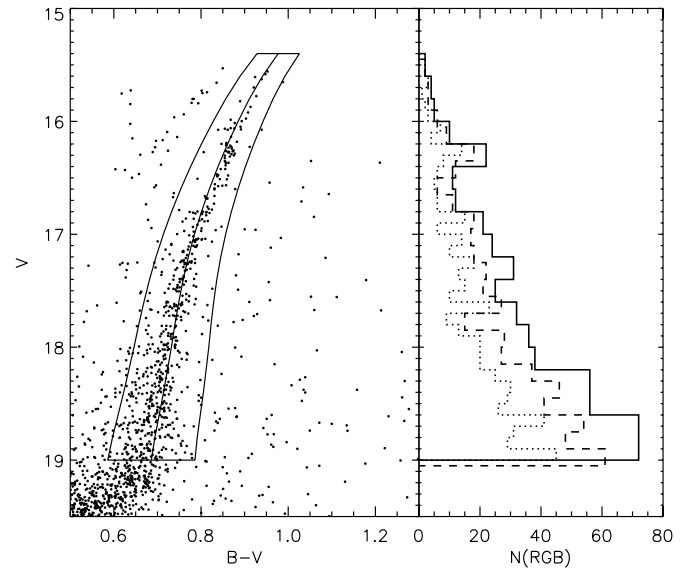

Figure 12. Enlargement of the RGB region of our CMD (left), showing all stars within half of the cluster tidal radius. The lines indicate the fiducial sequence of SD91, shifted redward in color by 0.01 as discussed in the text, as well as the swath used to select our initial RGB candidates. In our RGB luminosity function (right), solid lines correspond to a bin size of 0.2 mag, long dashed lines to 0.15 mag, and short dashed lines to 0.1 mag.

0.35 dex. The metallicities obtained from the RRc using this method are generally slightly lower than values obtained from other methods in both this study and those in the literature, but the uncertainties on these values are generally large and the Morgan et al. (2007) sample itself has a standard deviation of 0.145 dex. In the case of the three RRab, the light curves are generally of somewhat lower quality in which the maxima and minima are not both clearly observed, so rather than attempt to decompose their light curves, we have used the Fourier template-fitting code of Kovacs & Kupi (2007). Using the Jurcsik & Kovacs (1996) relation (which utilizes a sine series), we obtained [Fe/H] values of -1.60, -1.51 and -2.28 for the three RRab V3, V5, and V20, with rms deviations from the Fourier fits of 0.0233, 0.0057, and 0.0301, respectively. While this method allowed us to at least use the light curves of the RRab to obtain metallicity values, the practicality of this approach with such a small number of stars is debatable.

A fourth method for investigating the metallicity of NGC 6101 makes use of the difference between the HB magnitude and the magnitude of the bump in the RGB luminosity function (LF; Fusi Pecci et al. 1990). To create our RGB LF, we restricted our analysis to stars within half of the cluster tidal radius in an attempt to decontaminate our CMD of field stars while retaining enough RGB stars to use for our analysis. To construct a fiducial sequence, we used the sequence of SD91 as a starting point, shifting it redward by 0.01 in $B - V$ to match our data (this very slight color offset is also visible in Figure 2 of M01, and SD91 state that the zero points of their photometry are uncertain at the ~0.02 mag level). We then cut a swath around this fiducial, shown in Figure 12, to select initial RGB candidates, and we chose to set the width of the swath as 0.1 mag in $B - V$ at the base of the RGB ($V = 19$), decreasing linearly to 0.05 mag at our saturation limit of $V = 15.5$. To select RGB stars from these candidates, we divided the RGB into magnitude bins of equal size, and within each bin, the median photometric error in color was computed. Only stars within five times this median error in color were included in our final RGB LF. We found that

the initial width of our candidate "swath" had little influence on the final set of RGB stars, since it did not appreciably change the median color error in a given bin.

The RGB bump, discernible in the CMDs of SD91 and M01, is detected in our RGB LF, shown in Figure 12, as well. We have repeated the above analysis using three different bin sizes of 0.1, 0.15, and 0.2 mag in an attempt to constrain the location of the bump as much as possible. Using the smallest bin size, 0.1 mag, and the median magnitude in the bin where the bump occurs, we have determined that the magnitude of the bump is $V = 16.27 \pm 0.03$ mag, essentially identical to the M01 value of $V = 16.26 \pm 0.03$. We may now use the V magnitude difference between the HB and the bump as another metallicity determination. Using Equation (6.2) of Ferraro et al. (1999), which uses the ZW84 metallicity scale, and our value of $V_{\mathrm{BUMP}} - V_{\mathrm{ZAHB}} = -0.32 \pm 0.04$, we obtain $[\mathrm{Fe/H}] = -1.71 \pm 0.06$, slightly higher than previous literature values.

Metallicities obtained using the RRL, the HB, and the RGB on the CMD generally seem to agree well with previously determined values. If we calculate an average of the three values obtained from $(B - V)_{0,g}$ and the value obtained from the RGB bump, weighting them by the inverse of the squares of their uncertainties, we obtain $[\mathrm{Fe/H}] = -1.76 \pm 0.08$, in good agreement with recent estimates of $[\mathrm{Fe/H}] \approx -1.8$.

4.4. Oosterhoff Classification

We may determine the Oosterhoff type of NGC 6101 by examining the properties of its RRab and RRc. The mean periods of the RRL in this cluster are $\langle P_{ab} \rangle = 0.803$ days and $\langle P_c \rangle = 0.393$ days. Typical periods for Oosterhoff type II GGCs are $\langle P_{ab} \rangle = 0.64$ days and $\langle P_c \rangle = 0.38$ days (Smith 1995), with Oosterhoff type I clusters having shorter periods for both types of variables, indicating that NGC 6101 is Oosterhoff type II. Castellani et al. (2003, hereafter C03) divided GGCs with known RRL populations into groups by metallicity and found that clusters with $-2.0 < [\mathrm{Fe/H}] < -1.6$ constitute a gap in "RR Lyrae rich" GGCs. These clusters tend to occupy the Oosterhoff type II region on the Bailey diagram, and have small total numbers of RRL, which is related to the strong blue HB morphology seen in their CMDs. C03 then further subdivide these "RR Lyrae poor" clusters by metallicity. Their Group 1 is comprised of six clusters with $-1.85 \lesssim [\mathrm{Fe/H}] \lesssim -1.79$, similar to NGC 6101. Of these six clusters, three of them, NGC 4147, NGC 5897, and NGC 6809 (M55), have published periods and V-band amplitudes in the literature, from Stetson et al. (2005, hereafter SCS05), Clement & Rowe (2001), and Olech et al. (1999), respectively. Of these three clusters, we have chosen to exclude NGC 4147 for two reasons: first, SCS05 have classified it as Oosterhoff type I based on the mean periods of its RRab and RRc as well as their loci on the Bailey diagram. Second, and not unrelatedly, as SCS05 point out, recent metallicity estimates for NGC 4147 still cover a fairly wide range, extending considerably more metal-rich than the other clusters in Group 1 of C03. We have also reconsidered whether additional clusters should be included in the same metallicity group as NGC 6101 in light of the new metallicity scale of Carretta et al. (2009, hereafter C09), based on precise iron abundances for an unprecedented number of giants in GGCs. On their metallicity scale, NGC 6101 has $[\mathrm{Fe/H}] = -1.98 \pm 0.07$, and we have added the two clusters which harbor RRL with known V-band amplitudes and periods and have $[\mathrm{Fe/H}]$ values which are the same as NGC 6101 to within their uncertainties (in addition to the clusters mentioned above). These two clusters
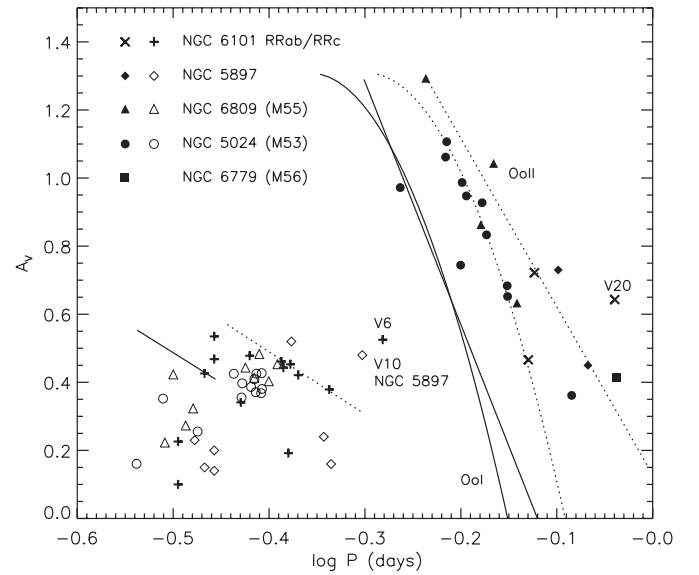

Figure 13. Bailey diagram for NGC 6101 and the other four GGCs with similar metallicities and available RRL V-band periods and amplitudes. For NGC 6101, RRab are shown as crosses and RRc as pluses, and for all other clusters, RRab are shown as filled symbols and RRc as open symbols: diamonds correspond to NGC 5897, triangles to M55, circles to M53, and the one M56 RRL with a known V-band period and amplitude is shown as a square. Solid and dotted lines represent fits to OoI and OoII RRL, respectively. The curved RRab fits and the RRc fits are from Cacciari et al. (2005) and Zorotovic et al. (2010), respectively. The linear Oo I and II fits for the RRab are from Clement (2000).

are M53 and M56, which have $[\mathrm{Fe/H}] = -2.06 \pm 0.09$ and -2.00 ± 0.09, respectively, on the C09 scale. However, of the nearly 60 RRL in M53, V-band periods and amplitudes are available for only 24 of them (Dékány & Kovács 2009), and of the three RRL in M56 (Wehlau & Sawyer Hogg 1985; Pietrukowicz et al. 2008), there is only one with a reliable V-band period and amplitude.

In Figure 13, we show the Bailey diagram for the RRL of NGC 6101, with the RRL of NGC 5897 and NGC 6809 (from Group 1 of C03) and M53 and M56 (included based on C09 $[\mathrm{Fe/H}]$ values) overplotted for comparison with clusters of similar metallicity. To aid in an Oosterhoff classification, Oosterhoff type I and II lines from Clement (2000), based on three GGCs, are overplotted, as well as those of Cacciari et al. (2005), which are based on the large RRL population of M3. Viewed in the context of GGC RRL populations, NGC 6101 is fairly similar to clusters with similar metallicities, with their RRab and RRc occupying roughly the same regions on the Bailey diagram, and indicating Oosterhoff type II. One of the most conspicuous features is V20, the primary cause of the large $\langle P_{ab} \rangle$ in NGC 6101. This RRab has an unusually large amplitude for its period, and as mentioned in Section 3.3, this amplitude should be viewed as a lower limit. Also notable is the variable V10 in NGC 5897, which appears close to our overluminous long-period RRc V6 in period–amplitude space. However, based on their CMD and light curves, Clement & Rowe (2001) surmised that this star may in fact be an anomalous Cepheid. This is unlikely to be the case for any of the luminous RRL in NGC 6101, since the faintest magnitude possible for anomalous and Population II Cepheids is over 1 mag brighter than the RRL at the metallicity of NGC 6101 (Caputo et al. 2004). Even if a field Cepheid happened to fall in our field of view, they would exhibit larger amplitudes than we detect for most of our RRL, as mentioned in the context of V17 in Section 3.3. Also notable is the presence of two RRL in our

sample, V21 and V22, which have periods and amplitudes which are smaller than the rest of the RRc. Clement & Rowe (2001) suggested that the four RRL in NGC 5897 which fall in this region of the Bailey diagram may in fact be second overtone pulsators. Some of the strongest observational evidence that these very short period, low amplitude RRL are second overtone pulsators, which have been designated RRe, is the existence of a second short period peak in the RRL period distributions of the Large and Small Magellanic Clouds distinct from that of the RRc (Alcock et al. 1996; Soszyński et al. 2009, 2010). While Alcock et al. (1996) suggest that the light curve shape may serve to further distinguish RRe from short period RRc, the latter two studies emphasize that the dividing line between RRc and RRe pulsators in terms of either the Bailey diagram or the Fourier parameters of the light curves is somewhat arbitrary. For this reason, we have included these stars in our sample of RRc in calculating mean periods and magnitudes.

With respect to the RRL population of NGC 6101 in general, the fraction of RRc is very large: $n(c)/n(ab + c) = 0.82$, well above the average of 0.46 for Oosterhoff type II GGCs (Smith 1995). A large fraction of RRc is to be expected to some extent since the metallicity of NGC 6101 is in the range of "RR Lyrae poor" GGCs which have higher values of $n(c)/n(ab + c)$ as discussed by C03. It may also be worth noting that this is also the highest fraction of RRc among all GGCs which harbor RRLs with known periods and amplitudes, although small number statistics obviously play a role.

4.5. Kinematics

Although the RRL population of NGC 6101 is reasonably akin to clusters with similar metallicities with regard to the period–amplitude distribution, this is not the case regarding its kinematics. The two most recent radial velocity studies of cluster giants, by Geisler et al. (1995) and Rutledge et al. (1997), found radial velocities for the cluster of 364.3 ± 1.9 km s^{-1} and 363.6 ± 10.6 km s^{-1}, respectively, providing very convincing evidence that the cluster exhibits retrograde motion around the Galactic center. This is contrary to the correlation between Oosterhoff type and the direction of cluster motion found by van den Bergh (1993a, 1993b), who discovered that, of clusters with known orbital parameters at that time, seven of the eight GGCs with known Oosterhoff types on retrograde orbits were Oosterhoff type I, and four of the five prograde clusters with Oosterhoff classifications were type II. Lee & Carney (1999) found the same pattern using a larger sample, although they found large velocity dispersions as well. Their results support the hypothesis of Rodgers & Paltoglou (1984) that lower metallicity clusters tend to have prograde orbits. More specifically, the clusters with retrograde orbits in fact occupy a particular metallicity range, $-1.65 \lesssim [\text{Fe/H}] \lesssim -1.3$, recently reinforced by Harris (1999) using a much improved data set. This correlation fits nicely into the classic galaxy formation theory advanced by Searle & Zinn (1978) that old halo clusters are closely tied to the early formation of the Milky Way, whereas the presence of younger, more metal-rich objects in the halo is due to later accretion and merger events. This scenario explains why the more metal-rich Oosterhoff type I GGCs have a much greater tendency to end up on retrograde orbits. The obvious question then becomes why NGC 6101, an old, fairly metal-poor cluster, is on a retrograde orbit, and the possible answers can give us some insight into its origin.

The key to understanding the origin of NGC 6101 may lie in the fact that it is not entirely alone in its unusual dynami-

cal properties: Mackey & Gilmore (2004) point out that there are two other old halo clusters that share its moderate ($R_{\text{GC}} \leqslant$ 11 kpc) galactocentric distance and large core radius ($R_{\text{core}} >$ 4.4 pc). Interestingly, these two clusters, M55 and NGC 5897, have very similar metallicities to NGC 6101, [Fe/H] = -1.81 and -1.80, respectively (H96). However, based on the GGC orbital motion study of Dinescu et al. (1999), neither of these clusters is on a retrograde orbit. Mackey & Gilmore suggest that the existence of these old clusters with relatively large cores in such proximity to the Galactic center could be explained by several survival mechanisms: They could be on wide orbits in which they spend minimal time near the Galactic center. Alternatively, they could be fairly recent additions to the halo itself from their parent galaxies. Since the cluster is old and hence quite different in CMD morphology from recent additions such as the Sagittarius clusters Arp 2 and Terzan 8, the most plausible of Mackey & Gilmore's suggestions may be that the cluster's original parent galaxy encountered dynamical friction with the dark matter halo of the Milky Way, causing it to end up on a small orbit before the cluster was released into the Galactic halo. Theoretical clues via dynamical simulations are provided by Martin et al. (2004), who simulate (to first order) the encounter between the Canis Major dwarf galaxy and the Milky Way. Their simulations include both a prograde and retrograde model, and they find that dynamically, NGC 6101 is very close in phase space to a cluster that would result from their retrograde model. However, this conclusion is highly circumstantial in that their prograde model is at least slightly more plausible.

An added curiosity is the inclusion of NGC 6101 as a candidate member of the MP-1 group of Fusi Pecci et al. (1995). They use radial velocities and Galactic longitude to tie GGCs to Milky Way satellites (the Magellanic clouds and stream in this case), and advance the concept that the origin of at least the relatively young GGCs may be connected to these satellites. However, NGC 6101 is fairly old and metal poor, and as they point out in regard to the three oldest and most metal-poor GGCs in the MP-1 group, the odds are high that their location in longitude–velocity space is a coincidence.

In summary, there are plausible explanations for the fact that NGC 6101 has kinematics which are atypical of its Oosterhoff classification, relating to its possible origin in a satellite dwarf galaxy. However, more detailed observations and simulations of Galactic dynamics are required to ascertain the history of this cluster more definitively.

5. CONCLUSIONS

We have used time-series photometry to study the RRL population of NGC 6101, and have confirmed 10 RRL candidates from Liller (1981) and identified seven new RRL. We can summarize the properties of the RRL population of NGC 6101 as follows.

1. The RRL population of NGC 6101 is typical of clusters with similar metallicities in that it has a small total number of RRL, and their mean periods and amplitudes are consistent with Oosterhoff type II. Most notably, at $n(c)/n(ab + c) = 0.82$, this cluster has the highest fraction of RRc known among GGCs.

2. We have detected one overluminous long-period RRc (V6) and one likely Blazhko RRab (V5). The observed fractions of these types of RRL in NGC 6101 are consistent with what has previously been found for GGCs.

3. A substantial fraction of the RRL are evolved, based on their locations on the CMD and synthetic ZAHB fits. If this is the case, the pulsational properties of the RRL are fairly consistent with previous determinations of the cluster metallicity and distance modulus. The observed width of the RRL magnitude distribution is relatively large, but not at significant odds with what is expected based on the cluster metallicity.

4. The retrograde motion of NGC 6101, unusual given its Oosterhoff classification, age, and metallicity, could be explained by the addition of the cluster to the Galactic halo from an accretion or merger event despite its proximity to the Galactic center.

REFERENCES

Alard, C. 2000, A&AS, 144, 363
Alcaino, G. 1974, A&AS, 18, 9
Alcock, C., et al. 1996, AJ, 111, 1146
Bono, G., Caputo, F., Castellani, V., & Marconi, M. 1997, A&AS, 121, 327
Bono, G., Caputo, F., & Stellingwerf, R. 1995, ApJS, 99, 263
Cacciari, C., Corwin, T. M., & Carney, B. W. 2005, AJ, 129, 267
Caputo, F., Castellani, V., Degl'Innocenti, S., Fiorentino, G., & Marconi, M. 2004, A&A, 424, 927
Carretta, E., Bragaglia, A., Gratton, R., D'Orazi, V., & Lucatello, S. 2009, A&A, 508, 695
Carretta, E., & Gratton, R. G. 1997, A&AS, 121, 95
Cassisi, S., & Salaris, M. 1997, MNRAS, 285, 593
Castellani, M., Caputo, F., & Castellani, V. 2003, A&A, 410, 871 (C03)
Catelan, M. 1992, A&A, 261, 443
Catelan, M. 2004, in ASP Conf. Ser. 310, Variable Stars in the Local Group, ed. D. W. Kurtz & K. R. Pollard (San Francisco, CA: ASP), 113
Chaboyer, B. 1999, in Post Hipparcos Cosmic Candles, ed. A. Heck & F. Caputo (Dordrecht: Kluwer), 111
Clement, C. 2000, in ASP Conf. Ser. 203, The Impact of Large-Scale Surveys on Pulsating Star Research, ed. L. Szabados & D. Kurtz (San Francisco, CA: ASP), 266
Clement, C., et al. 2001, AJ, 122, 2587
Clement, C., & Rowe, J. 2001, AJ, 122, 1464
Clementini, G. 2010, in Proc. Int. Conf. on Variable Stars, the Galactic halo and Galaxy Formation, ed. C. Sterken, N. Samus, & L. Szabados (Russia: Sternberg Astronomical Institute, Moscow Univ.)
Clementini, G., Federici, L., Corsi, C., Cacciari, C., Ballazzini, M., & Smith, H. A. 2001, ApJ, 559, 109
Corwin, T. M., & Carney, B. W. 2001, AJ, 122, 3183
Dékány, I., & Kovács, G. 2009, A&A, 507, 803
Dinescu, D. I., Girard, T. M., & van Altena, W. F. 1999, AJ, 117, 1792
Dotter, A., Chaboyer, B., Jevremović, D., Kostov, V., Baron, E., & Ferguson, J. W. 2008, ApJS, 178, 89
Dotter, A., et al. 2010, ApJ, 708, 698
Ferraro, F. R., Messineo, M., Fusi Pecci, F., de Palo, M. A., Straniero, O., Chieffi, A., & Limongi, M. 1999, AJ, 118, 1738

Fusi Pecci, F., Ballazzini, M., Cacciari, C., & Ferraro, F. R. 1995, AJ, 110, 1664
Fusi Pecci, F., Ferraro, F. R., Crocker, D. A., Rood, R. T., & Buonanno, R. 1990, A&A, 238, 95
Geisler, D., Piatti, A. E., Claria, J. J., & Minniti, D. 1995, AJ, 109, 605
Gilliland, R. L., & Brown, T. M. 1988, PASP, 100, 754
Harris, W. E. 1996, AJ, 112, 1487 (H96)
Harris, W. E. 1999, in Globular Clusters, ed. C. Martinez Roger (Cambridge: Cambridge Univ. Press)
Jurcsik, J., et al. 2009, MNRAS, 400, 1006
Jurcsik, K., & Kovacs, G. 1996, A&A, 312, 111
Kolenberg, K., et al. 2010, ApJ, 713, L198
Kovacs, G., & Kupi, G. 2007, A&A, 462, 1007
Landolt, A. U. 1992, AJ, 104, 340
Lee, J.-W., & Carney, B. W. 1999, AJ, 118, 1373
Liller, M. H. 1981, AJ, 86, 1204
Mackey, A. D., & Gilmore, G. F. 2004, MNRAS, 355, 504
Marconi, G., Andreuzzi, G., Pulone, L., Cassisi, S., Testa, V., & Buonanno, R. 2001, A&A, 380, 478 (M01)
Martin, N., Ibata, R. A., Bellazzini, M., Irwin, M. J., Lewis, G. F., & Dehnen, W. 2004, MNRAS, 348, 12
Morgan, S. M., Wahl, J. N., & Wieckhorst, R. M. 2007, MNRAS, 374, 1421
Moskalik, P., & Poretti, E. 2003, A&A, 398, 213
Olech, A., Kaluzny, J., Thompson, I. B., Pych, W., Krzeminski, W., & Schwarzenberg-Czerny, A. 1999, AJ, 118, 442
Piersimoni, A. M., Bono, G., & Ripepi, V. 2002, AJ, 124, 1528
Pietrukowicz, P., Olech, A., Kedzierski, P., Zloczewski, K., Wisniewski, M., & Mularczyk, K. 2008, Acta Astron., 58, 121
Piotto, G., et al. 2002, A&A, 391, 945
Rodgers, A. W., & Paltoglou, G. 1984, ApJ, 283, L5
Rosenberg, A., Piotto, G., Saviane, I., & Aparicio, A. 2000, A&AS, 144, 5
Rutledge, G. A., Hesser, J. E., Stetson, P. B., Mateo, M., Simard, L., Bolte, M., Friel, E. D., & Copin, Y. 1997, PASP, 109, 883
Sandage, A. 1990, AJ, 350, 631
Sandage, A. 1993, AJ, 106, 687
Sandage, A. 2004, AJ, 128, 858
Sandage, A. 2006, AJ, 131, 1750
Sarajedini, A., Barker, M. K., Geisler, D., Harding, P., & Schommer, R. 2006, AJ, 132, 1361
Sarajedini, A., & Da Costa, G. S. 1991, AJ, 102, 628 (SD91)
Sarajedini, A., & Layden, A. 1997, AJ, 113, 264
Sarajedini, A., Mancone, C. L., Lauer, T. R., Dressler, A., Freedman, W., Trager, S. C., Grillmair, C., & Mighell, K. J. 2009, AJ, 138, 184
Sarajedini, A., et al. 2007, AJ, 133, 1658
Schlegel, D. J., Finkbeiner, D. P., & Davis, M. 1998, ApJ, 500, 525
Searle, L., & Zinn, R. 1978, ApJ, 225, 357
Smith, H. A. 1995, RR Lyrae Stars (Cambridge: Cambridge Univ. Press)
Soszyński, I., Udalski, A., Szymański, M. K., Kubiak, M., Pietrzyński, G., Wyrzykowski, L., Ulaczyk, K., & Poleski, R. 2010, Acta Astron., 60, 165
Soszyński, I., et al. 2008, Acta Astron., 58, 293
Soszyński, I., et al. 2009, Acta Astron., 59, 1
Stetson, P. B. 1987, PASP, 99, 191
Stetson, P. B., Catelan, M., & Smith, H. A. 2005, PASP, 117, 1325 (SCS05)
Székely, P., Kiss, L. L., Jackson, R., Derakas, A., Csák, B., & Szatmáry, K. 2007, A&A, 463, 589
Tammann, G. A., Sandage, A., & Reindl, B. 2008, ApJ, 679, 52
van den Bergh, S. 1993a, MNRAS, 262, 577
van den Bergh, S. 1993b, AJ, 105, 971
VandenBerg, D. A., & Clem, J. L. 2003, AJ, 126, 778
VandenBerg, D. A., Bergbusch, P. A., & Dowler, P. D. 2006, ApJS, 162, 375
Wehlau, A., & Hogg, H. S. 1985, AJ, 90, 2514
Zinn, R., & West, M. J. 1984, ApJS, 55, 45
Zorotovic, M., et al. 2010, AJ, 139, 357